

Frequency control in the process of a multicell superconducting cavity production

Valery Shemelin and Paul Carriere

Citation: *Rev. Sci. Instrum.* **83**, 043304 (2012); doi: 10.1063/1.4705985

View online: <http://dx.doi.org/10.1063/1.4705985>

View Table of Contents: <http://rsi.aip.org/resource/1/RSINAK/v83/i4>

Published by the [American Institute of Physics](#).

Related Articles

A polyvalent harmonic coil testing method for small-aperture magnets

Rev. Sci. Instrum. **83**, 085116 (2012)

A new compact, high sensitivity neutron imaging system

Rev. Sci. Instrum. **83**, 10E131 (2012)

Generation of a beam of fast electrons by tightly focusing a radially polarized ultrashort laser pulse

Appl. Phys. Lett. **101**, 041105 (2012)

The various manifestations of collisionless dissipation in wave propagation

Phys. Plasmas **19**, 063110 (2012)

Experimental investigation on focusing characteristics of a He-Ne laser using circular Fresnel zone plate for high-precision alignment of linear accelerators

Rev. Sci. Instrum. **83**, 053301 (2012)

Additional information on *Rev. Sci. Instrum.*

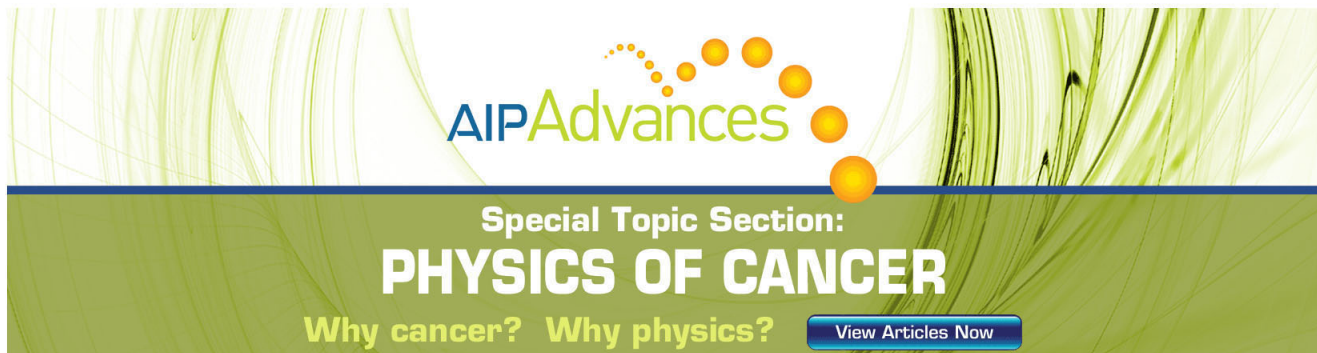
Journal Homepage: <http://rsi.aip.org>

Journal Information: http://rsi.aip.org/about/about_the_journal

Top downloads: http://rsi.aip.org/features/most_downloaded

Information for Authors: <http://rsi.aip.org/authors>

ADVERTISEMENT



AIP Advances

Special Topic Section:
PHYSICS OF CANCER

Why cancer? Why physics? [View Articles Now](#)

Frequency control in the process of a multicell superconducting cavity production

Valery Shemelin^{a)} and Paul Carriere

Cornell Laboratory for Accelerator-based Sciences and Education (CLASSE), Ithaca, New York 14853, USA

(Received 5 March 2012; accepted 9 April 2012; published online 26 April 2012)

Modifications in the geometry of a superconducting RF cavity due to various processing procedures are presented in a convenient matrix formulation. Specifically, the effect of chemical etching, cooling down, and preloading are characterized, while the corresponding frequency shifts are calculated with a reliable software. This matrix method was used in the fabrication of the first Cornell energy recovery linac (ERL) 7-cell cavity. Cavity fabrication can be broken down into three main stages: deep-drawing cups, welding the cups in pairs to obtain “dumbbells” and end groups, and, finally, welding the obtained components into a completed cavity. Frequency measurements and precise machining were implemented after the second stage. A custom RF fixture and data acquisition system were designed and validated for this purpose. The system comprised of a mechanical press with RF contacts, a network analyzer, a load cell and custom LABVIEW and MATLAB scripts. To extract the individual frequencies of the cups from these measurements, the established algorithm of calculations was analysed and corrected. Corrections for the ambient environment were also incorporated into the measurement protocol. Using the procedure presented, the frequency deviation of the completed 1.3 GHz 7-cell cavity was 360 kHz, corresponding to an average error about 75 μm in length for every cell. © 2012 American Institute of Physics. [<http://dx.doi.org/10.1063/1.4705985>]

INTRODUCTION

Optimization of the accelerating superconducting cavity shape consists in a search of the shape in its final superconducting state. This raises the question of how the elliptic arc definition of cavities is modified during fabrication. Maintaining cavity shape is important not only for limitation of maximal electric and magnetic fields, but it is also crucial to achieving a minimized BBU parameter, since the higher order modes responsible for beam break up are even more sensitive to geometric distortions than the fundamental TM_{010} mode. A robust design should account for all processing procedures including etching, thermal contraction and frequency tuner preload (axial preloading is needed to minimize frequency tuner motor backlash) since we expect these steps to modify the microwave properties of our resonator. A convenient way to depict the cavity shape and technological operations changing this shape is a matrix presentation of an elliptic multicell accelerating cavity described below.

Production of the first superconducting (SC) cavities for the Cornell University energy recovery linac (ERL) is complete. In the initial stage of fabrication, we encountered an issue regarding frequency control of individual cells when the half-cells (or cups) are welded together to form “a dumbbell.” Because of a non-ideal shape of the cups and not fully controlled shrinkage of material by welding the cups are intentionally manufactured with some extra length on the equator which should be trimmed in the following processing. We used a wealth of experience in the fabrication of SC cavities described in DESY and JLab publications.¹⁻³

Both labs used measuring fixtures with a perturbing body to identify a possible asymmetry of the dumbbell. There is no direct reference in the DESY publications how this asymmetry is used to define the individual cup frequencies, but in the JLab publication, the measured frequencies with and without perturbation were used for the definition of the π -mode frequencies of the cups. Some corrections to the formulae for calculation of these frequencies and description of the dumbbell measurements are given in the second part of this paper.

MATRIX DESCRIPTION OF THE CAVITY SHAPE

Superconducting RF cavity shape is commonly defined by a series of elliptical arcs connected with tangent segments, as shown in Figure 1.

So, a full description of the final dimensions of a cavity excluding the lengths of end pipes can be explicitly presented as

$$\text{dim}_f = \begin{pmatrix} x_1 & x_2 & \cdots & x_n \\ y_1 & y_2 & \cdots & y_n \\ a_1 & a_2 & \cdots & a_n \\ b_1 & b_2 & \cdots & b_n \end{pmatrix}.$$

“Final” refers to the cavity when it has had a surface preparation (etching and, possibly, tumbling), preloading and cryogenic cooling down. In the first line of the matrix are longitudinal coordinates of the centres of the elliptic arcs, in the second line – the radial coordinates of the centres, in the third and fourth – longitudinal and radial half-axes of the ellipses, respectively.

^{a)}Electronic mail: vs65@cornell.edu.

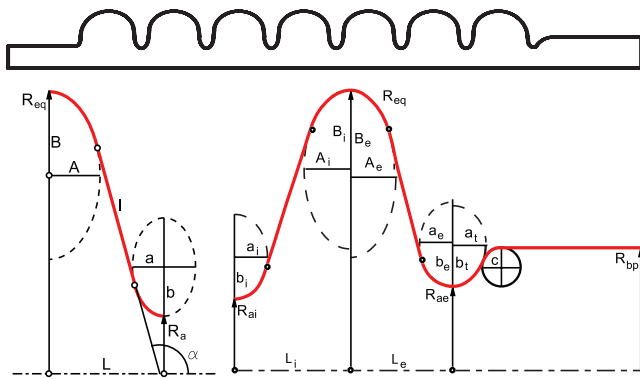


FIG. 1. A multicell cavity (upper picture) and its presentation as a chain of elliptic arcs connected with straight segments: inner half-cell and end cell (lower pictures). End cells can have an additional iris: compare the right and left ends.

If shrinkage only due to niobium thermal contraction from 293 K to 0 K is considered,⁴ the starting dimensions of the cavity should be bigger by the factor of $1 + kT = 1 + 1.43 \times 10^{-3}$.⁵

$$\dim_s = \dim_f \cdot (1 + kT).$$

Similarly, if only etching is taken into account, then

$$\dim_s = \dim_f - \text{Etch},$$

where the matrix Etch is defined by

$$\text{Etch} = \begin{pmatrix} 0 & 0 & \dots & 0 \\ 0 & 0 & \dots & 0 \\ ex1 & ex2 & \dots & exn \\ ey1 & ey2 & \dots & eyn \end{pmatrix},$$

where positive values in the third and fourth rows correspond to concave surfaces (equatorial ellipses) and negative values of ex and ey are for decreasing half-axes (irises). This formulation allows us to account for different values of etching for equatorial and iris regions if they are known from experiment (different ellipses = different columns) and even for lower and upper parts of the ellipses (for different axes = different rows).

If only compression (or stretching) of the cavity is considered, we can write

$$\dim_s = \dim_f - P \cdot \Delta L,$$

where P is the matrix of ‘‘pliability’’:

$$P = \begin{pmatrix} px1 & px2^* & \dots & pxn^* \\ py1 & py2 & \dots & pyn \\ pa1 & pa2 & \dots & pan \\ pb1 & pb2 & \dots & pbn \end{pmatrix},$$

$px1, py1, pa1, pb1$, and so on are coefficients in the relations: $\Delta x1 = px1 \cdot \Delta L$, $\Delta y1 = py1 \cdot \Delta L$, $\Delta a1 = pa1 \cdot \Delta L$, $\Delta b1 = pb1 \cdot \Delta L$, and so on. ΔL is total compression of the cavity. $\Delta x1, \Delta y1, \Delta a1, \Delta b1, \dots$ are changes in the corresponding coordinates and axes lengths. Asterisks designate the cumulative values: $px2^* = px1 + px2$, $px3^* = px2^* + px3$, and so on.

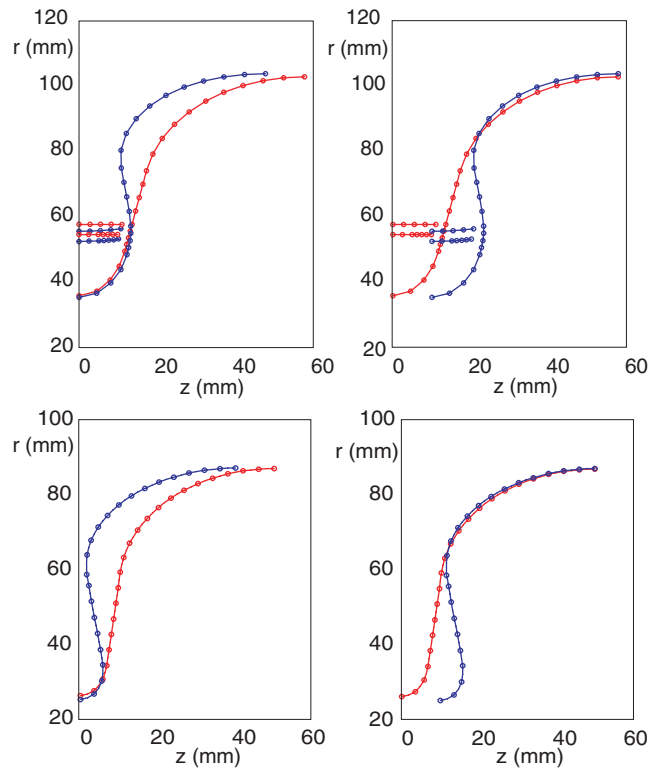


FIG. 2. Deformation of the inner half-cell of the Cornell ERL cavity (with stiffening rings, upper pictures) and of the low loss cavity of the Jefferson Lab.³ Wall thickness in simulation is 3 mm. Outer surface of the cavities is not shown. The deformation of $\Delta L = 10 \mu\text{m}$ is magnified $\times 1000$.

Since all the corrections are small, we take into account the first order only and unite them in the final formula

$$\dim_s = \dim_f \cdot (1 + kT) - \text{Etch} - P \cdot \Delta L.$$

CONSERVATION OF THE ELLIPTIC SHAPE

In the previous derivation, we assumed that the elliptical definition of a cavity is maintained. This assumption is motivated by the relatively small changes of dimensions incurred during technological operation. Nevertheless, we present simulated data for deformation due to cavity tuning (i.e. axial loading). Simulations were done⁶ for the Cornell ERL and for the JLab low loss cavity.³ There are no stiffening rings in the LL cavities⁷ and its deformation is quite different from the cavity with stiffeners.

Results of the simulation are presented in Figure 2 and in Table I. By fixing the left-most or the right-most point of the half-cell at place (left and the right images respectively) one can see that deformations of the equatorial and iris regions are small and the most part of deformation consists in tilting of the tangent line segment connecting the elliptic arcs. It is seen that the stiffening ring also noticeably deforms. The effect of shortening the cavity (as is shown on the picture, $\Delta L < 0$) on the other dimensions of the Cornell and JLab multicell cavities inner cell is presented in Table I (see lower left portion of Figure 1 for inner cell designations).

One can also note that tuning to the desired frequency occurs not because of change of the equatorial radius as is stated

TABLE I. Coefficients of the P matrix for the inner cell and relative deformation of the equator and iris radii; designations for the geometric parameters ($A, B, a, b, L, R_{eq}, R_a$) – see Figure 1 (lower left); x_1, y_1, x_2, y_2 are coordinates of the ellipses centres.

	Equator area		Iris area	
	Cornell ERL cavity	JLab LL cavity	Cornell ERL cavity	JLab LL cavity
$px_1 = \Delta x_1 / \Delta L$	0	0	$px_2 = \Delta x_2 / \Delta L$	1
$py_1 = \Delta y_1 / \Delta L$	-1.134	-0.553	$py_2 = \Delta y_2 / \Delta L$	0.038
$pA = \Delta A / \Delta L$	0.415	0.15	$pa = \Delta a / \Delta L$	-0.076
$pB = \Delta B / \Delta L$	1.027	0.549	$pb = \Delta b / \Delta L$	-0.010
$\Delta R_{eq} / \Delta L = py_1 + pB$	-0.107	-0.004	$\Delta R_a / \Delta L = py_2 - pb$	0.048

in Ref. 3 but mainly because of change of the wall slope angle resulting in a decreased distance between irises and, therefore, change in capacitance. The increase of the equator radius also decreases the frequency and this contribution is about 30% (calculated with SLANS) in the case of the Cornell ERL cavity with stiffening rings but is much smaller for a cavity without stiffening rings as can be seen from the picture and the table. The presence of the rings increases deformation of the equatorial radius but this deformation is practically zero in the absence of rings.

Physically, it is reasonable because the force needed to stretch/squeeze the belt between two planes parallel to the equator plane and spaced, say, 1 cm from the equator, along its length is much bigger than the force needed to bend the cavity slanted wall even though a part of this wall is fixed with a stiffening ring.

After deformation the elliptic shape of the equatorial and the iris area is maintained, Figure 3. Moreover, the straight segment is tangent to the arcs as before with a good accuracy. To quantify the deformation we define the normalized root-mean-square deviation (NRMSD) of the deformed shape from the changed ellipse,

$$\text{NRMSD} = \frac{\text{RMSD}}{R_{max} - R_{min}}.$$

For the equator elliptic arc, in the case of the Cornell ERL cavity, NRMSD is 1.2% while for the iris arc it is found to be 1.1%. Here, the root-mean-square deviation, RMSD, is de-

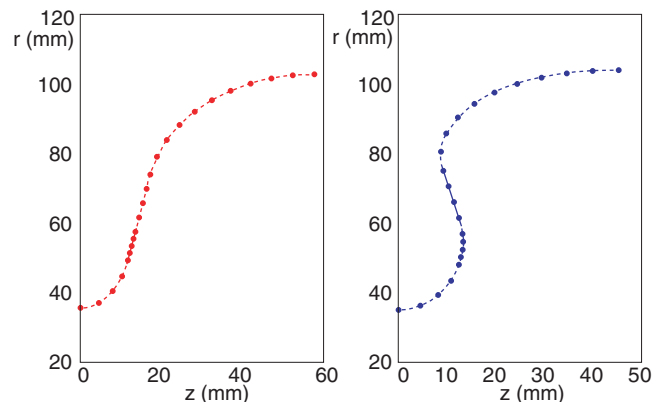


FIG. 3. After deformation the cell keeps elliptic arcs with a straight segment between them.

finied as

$$\text{RMSD}(R_{e,i} - R_{a,i}) = \sqrt{\frac{\sum_{i=1}^n (R_{e,i} - R_{a,i})^2}{n}},$$

where R_{max} and R_{min} are the limits of the arcs in the radial direction, $R_{e,i}$ and $R_{a,i}$ are radii at the points along the elliptic arcs and on the “actual” arcs calculated by ANSYS, respectively. The number of points, n , in this example is 11 for the upper arc and 10 for the lower elliptic arc as is shown in Figure 3. Let us restate that these deviations of the arcs are also magnified 1000 times, and actually the elliptic shapes deviate by approximately 0.001% rms.

Measurements done with the Zeiss coordinate measuring machine show that real deviation from the elliptic shape after fabrication may run as high as 100 – 200 μm .⁸

With the end plates fixed, the sensitivity of the cavity to differential pressure between the inner vacuum and outside wall (atmosphere or liquid helium) is about 1 Hz per millibar, or 1 kHz per atmosphere,⁶ and is negligible compared to the axial loading.

In the case of the ERL inner cell, the sensitivity to axial loading is 300 kHz/52 μm . The value of 300 kHz can be sufficient for preloading. Cooling down will change the dimensions up to 150 μm (equatorial radius), and etching is about 150–200 μm (sometimes light etching is used after the usual etching procedure). All these values are of the same order of magnitude but the deformation from the mechanical tuning is the smallest compared to changes of dimensions due to etching and cooling. It is smaller than accuracy of fabrication (we expected 200–500 μm for the whole cavity) and in the case of the ERL we neglected this correction, i.e. we assumed the matrix $P = 0$. However, in some cases, when no stiffening rings are used or higher preloading is required, this deformation can be bigger and should be accounted.

Consideration and correction of different geometrical deviations are also insightful for understanding of the position and properties of higher order modes.

USAGE OF THE MATRIX APPROACH TO THE ERL MULTICELL CAVITY

Dimensions of the ERL 7-cell cavity cells were optimized taking into account different constraints.⁹ The final dimensions (in mm) of this cavity can be presented in the matrix

form

$$\text{dim}_f = \left(\begin{array}{cccc|cc|cccc} 318.54 & 354.42 & 354.42 & 412.42 & 0 & 57.65 & 1104.25 & 1161.39 & 1161.39 & 1197.26 \\ 19 & 56.95 & 60.30 & 62.35 & 67.31 & 57.12 & 62.35 & 60.03 & 56.96 & 19 \\ 36 & 11.27 & 12.49 & 41.51 & 41.35 & 12.35 & 40.91 & 12.57 & 11.28 & 36 \\ 36 & 20.95 & 24.30 & 40.53 & 35.57 & 21.14 & 40.53 & 24.02 & 20.95 & 36 \end{array} \right).$$

We have not repeated the inner half-cells dimensions 12 times with a constant shift in the first line and mirror reflections of the adjacent half-cells, so one only central half-cell is presented in the fifth and sixth columns. Conditionally, the origin *z*-coordinate here is taken equal to 0. The left and right end groups are described in the first and last four columns respectively. Both end groups have an additional iris like in Figure 1 (lower right) and consist of 3 elliptic and 1 circular arc, so need 4 columns for their description.

Etching of the cavity (BCP and EP) was performed in several steps. The cavity orientation was changed several times: each end was alternatively the upper and the lower end in this procedure. So, we tried to achieve as uniform etching as possible. Ultrasonic measurements¹⁰ of the material removal were evaluated as 143 μm with the standard deviation of 37 μm (26%). These measurements were taken at each flat section on the cell, and just above and below the equator. The deviations in the iris area can be higher but the sensitivity of

frequency to the change of dimensions in this area is lower and is less important. The matrix approach has a potential to introduce difference in etching depth for the iris and the equator area but we did not do this in our calculations.

With regard to thermal contraction (1.43×10^{-3}) and uniform etching of all the surfaces by $\Delta = 150 \mu\text{m}$ we have

$$\text{dim}_s = \text{dim}_f \cdot (1 + kT) - \text{Etch},$$

where

Etch

$$= \left(\begin{array}{cccc|cc|cccc} 0 & 0 & 0 & 0 & 0 & 0 & 0 & 0 & 0 & 0 \\ 0 & 0 & 0 & 0 & 0 & 0 & 0 & 0 & 0 & 0 \\ 1 & -1 & -1 & 1 & 1 & -1 & 1 & -1 & -1 & 1 \\ 1 & -1 & -1 & 1 & 1 & -1 & 1 & -1 & -1 & 1 \end{array} \right) \cdot \Delta,$$

therefore, the compensated dimensions for the cavity production are

$$\text{dim}_s = \left(\begin{array}{cccc|cc|cccc} 319.01 & 354.93 & 354.93 & 413.01 & 0 & 57.74 & 1105.83 & 1163.05 & 1163.05 & 1198.97 \\ 19.03 & 57.03 & 60.39 & 62.44 & 67.41 & 57.20 & 62.44 & 60.12 & 57.04 & 19.03 \\ 35.90 & 11.44 & 12.66 & 41.42 & 41.26 & 12.52 & 40.82 & 12.74 & 11.44 & 35.90 \\ 35.90 & 21.13 & 24.48 & 40.44 & 35.47 & 21.32 & 40.44 & 24.21 & 21.13 & 35.90 \end{array} \right).$$

A small difference of the end irises outer elliptic arcs can be neglected because it is less than accuracy of production and the elliptic arc center radial coordinate can be taken as 57.04 mm for both irises. Besides, the initial radius of the beam pipe is 55 mm, and it should coincide with the sum of the end iris radius (now 35.90) and the position of its center (19.03). However, there is no neces-

sity to strictly keep the circle radius of 36 mm or its center position as the final dimensions because this circle is chosen for multipactor preventing¹¹ and can be varied in a wide range. In this case, we need only to correct the *z*-coordinates of the extreme circles. After all these corrections, the matrix of dimensions for the production drawings becomes

$$\text{dim}_s = \left(\begin{array}{cccc|cc|cccc} 318.91 & 354.93 & 354.93 & 413.01 & 0 & 57.74 & 1105.83 & 1163.05 & 1163.05 & 1199.07 \\ 19 & 57.04 & 60.39 & 62.44 & 67.41 & 57.20 & 62.44 & 60.12 & 57.04 & 19 \\ 36 & 11.44 & 12.66 & 41.42 & 41.26 & 12.52 & 40.82 & 12.74 & 11.44 & 36 \\ 36 & 21.13 & 24.48 & 40.44 & 35.47 & 21.32 & 40.44 & 24.21 & 21.13 & 36 \end{array} \right) \tag{1}$$

CORRECTION FOR MEASUREMENT CONDITIONS

Using SLANS,¹² the calculated resonant frequency of the central cell defined by matrix (1) is $f_{calc} = 1299.655$ MHz. This is a frequency at room temperature ($T_0 = 293$ K) but without regard for dielectric permittivity of air. ε of air depends on the atmospheric pressure p , humidity φ , and temperature T (Ref. 13)

$$\varepsilon = 1 + 210 \cdot 10^{-6} \frac{p}{T} + \varphi \frac{p_{sv}}{T} \left(\frac{10040}{T} - 0.30 \right) \times 10^{-6} \quad (2)$$

Here p and p_{sv} are measured in mm Hg, T - Kelvin, φ - %. In this formula compared to the original one, the change is made from p_{air} to $p_{air} = p - p_{sv} \cdot \varphi/100$, where p_{sv} is the water's vapour saturated pressure at the given temperature, so that the directly measured atmospheric pressure can be used. Instead of an inconvenient table, p_{sv} can be approximated¹⁴ by

$$\log p_{sv} = 7.45 \cdot \frac{T - 273}{T - 38.3} + 0.656, \quad (3)$$

which very well coincides (Figure 4) with table data used in Ref. 3.

The frequency measured in atmosphere will differ from calculated by SLANS

$$f_{meas} = \frac{f_{calc}}{[1 + \alpha(T - T_0)]\sqrt{\varepsilon}}$$

where $\alpha = 7.3 \times 10^{-6} \text{ K}^{-1}$ is the thermal expansion coefficient of niobium at room temperature, $T_0 = 293$ K.

ε in Eq. (2) can be simplified for small deviations from normal conditions ($p = 760$ mm Hg, humidity = 50%, $T = T_0$):

$$\varepsilon = \varepsilon_{nc} + (0.72 \cdot \Delta p + 3.8 \cdot \Delta T + 2.0 \cdot \Delta \varphi) \times 10^{-6},$$

$$\varepsilon_{nc} = 1.000646.$$

Taking into account both thermal expansion and variation of ε , we have

$$f_{meas} = f_{calc} / [1 + (343 + 9.2\Delta T + 0.36\Delta p + 1.0\Delta \varphi) \times 10^{-6}].$$

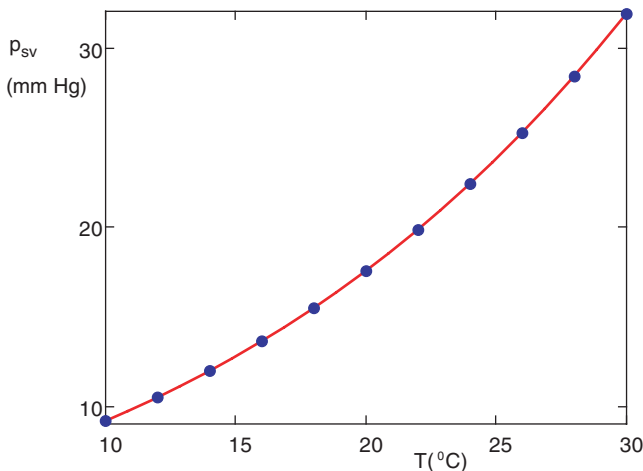


FIG. 4. Pressure of saturated vapor of water. Comparison of data from formula (3) (line) and from the table used in Ref. 3 (dots).

For $\Delta T = \Delta p = \Delta \varphi = 0$,

$$f_{meas} = 1299.234 \quad \text{if} \quad f_{calc} = 1299.655 \text{ MHz.}$$

For reference, $\Delta f = 10$ kHz, if $\Delta T = 0.84^\circ\text{C}$, or $\Delta p = 21.4$ mm Hg, or $\Delta \varphi = 7.7\%$.

If we take into account the mechanical preloading, for example, preliminary stretching for 300 kHz, then the target frequency becomes $f_{target} = 1298.934$ MHz. The mechanical preloading was neglected in our design, therefore we do not expect the dimensions listed in (1) to result in a final frequency of 1300 MHz after etching, cooling down and preloading.

As previously mentioned, the half-cells are fabricated with some extra length in the equatorial region, such that this length can be fitted to tune the cell to the desired frequency.

To find the target frequency of our measurements at normal conditions we can calculate the frequency value for each state of the cavity (in MHz):

Vacuum, 2 K, tuned 300 kHz (stretched)	1300.000
Before tuning	1299.700
All the same but at 20°C (divide by 1.00143)	1297.844
In air: 20°C, 50% rel. humidity, 760 mm Hg (divide by 1.000323)	1297.425
Before BCP (1560 kHz/150 μm)	1298.985

This value

$$f_{target} = 1298.985 \text{ MHz}$$

was taken for measurements with consequent correction for deviation of ambience from normal conditions.

A FORMULA FOR CALCULATION THE FREQUENCIES OF THE INDIVIDUAL HALF-CELLS OF DUMBBELL

Symmetrization of the formula

The formula for the calculating the individual resonances of two coupled oscillators used by Ref. 3 is derived in Refs. 15 and 16:

$$f_{\pi,U} = \sqrt{\frac{f_{\pi}^2 + f_0^2}{2} + \frac{(f_{\pi}^2 - f_0^2) \cdot (2 + R)}{2\sqrt{R+4}}}, \quad (4)$$

$$f_{\pi,D} = \sqrt{\frac{f_{\pi}^2 + f_0^2}{2} + \frac{(f_{\pi}^2 - f_0^2) \cdot (2 - R)}{2\sqrt{R+4}}},$$

with the substitution

$$R = \sqrt{\frac{f_{\pi}^2 - f_{\pi,P,U}^2}{f_{\pi}^2 - f_{\pi,P,D}^2}} - \sqrt{\frac{f_0^2 - f_{0,P,U}^2}{f_0^2 - f_{0,P,D}^2}}. \quad (5)$$

Here “0” and “ π ” denote the 0-mode or π -mode respectively and half-cells are distinguished by their location in the fixture with indices “U” for up and “D” for down. Dumbbell mode frequencies with the perturbation object are additionally marked with an index “P.” One can see that both Eqs. (4) and (5) are asymmetric relative to a swap of indices “U” and “D”. Analysis of the derivation of the formula in Ref. 15 shows that there should be R^2 in the denominators

of Eq. (4)

$$f_{\pi,U}^* = \sqrt{\frac{f_{\pi}^2 + f_0^2}{2} + \frac{(f_{\pi}^2 - f_0^2) \cdot (2 + R)}{2\sqrt{R^2 + 4}}}, \quad (6)$$

$$f_{\pi,D}^* = \sqrt{\frac{f_{\pi}^2 + f_0^2}{2} + \frac{(f_{\pi}^2 - f_0^2) \cdot (2 - R)}{2\sqrt{R^2 + 4}}}.$$

Now formulae in Eq. (6) are symmetric if R in Eq. (5) changes its sign when the dumbbell is turned upside-down. However, this can happen only if both right components in Eq. (5) are close to a unity

$$R = \sqrt{\frac{f_{\pi}^2 - f_{\pi,P,U}^2}{f_{\pi}^2 - f_{\pi,P,D}^2}} - \sqrt{\frac{f_0^2 - f_{0,P,U}^2}{f_0^2 - f_{0,P,D}^2}} \approx (1 + \alpha) - (1 + \beta) = \alpha - \beta, \quad (7)$$

$$R' = \sqrt{\frac{f_{\pi}^2 - f_{\pi,P,D}^2}{f_{\pi}^2 - f_{\pi,P,U}^2}} - \sqrt{\frac{f_0^2 - f_{0,P,D}^2}{f_0^2 - f_{0,P,U}^2}} \approx \frac{1}{1 + \alpha} - \frac{1}{1 + \beta} \approx \beta - \alpha \approx -R.$$

This, in its turn, can happen when the shift caused by the extra length of the cell is less than the shift due to perturbation.

One could transform the formula for R so that it would be symmetrical, e. g., by taking a mean arithmetic of R and $-R'$, or using an expansion by the small parameter mentioned above. But the original formula (5) is rather compact and the transformed formula would be presumably more cumbersome and hardly more accurate. Let us first check formulae (5) and (6) with a dumbbell having a given extra length of each cup. This check can be done with SLANS.¹² We will believe that SLANS gives exact values of frequencies for the original dumbbell and the dumbbells with perturbations. We can also find the sensitivity of the π -mode of an individual cup to the added extra length, referred to as the trimming parameter, t . In our case it appeared that $t = 5.1$ MHz/mm. Knowing the frequency of an “ideal” cup or the target frequency, f_{target} , we can find the extra lengths

$$\Delta_U = \frac{f_{target} - f_{\pi,U}^*}{t}, \text{ and } \Delta_D = \frac{f_{target} - f_{\pi,D}^*}{t} \quad (8)$$

to be trimmed. This allows us to compare SLANS results with the results of formulae (6). We can also analyze how errors of the measurements of the dumbbell frequencies influence on the accuracy of the found extra length. For this purpose, we can generate random values of frequencies around the values calculated by SLANS and again use the formulae (5) and (6) but now for 6 arrays of “measured” frequencies. Our measurements show that the standard deviation of each of 6 measured frequencies (see Eq. (5)) is about $\sigma = 10$ kHz. Let the dumbbell has an extra lengths from one side only: $\Delta_1 = 1$ mm, $\Delta_2 = 0$. The perturbation in this calculation was taken of such a size that it makes frequency shift of the π -mode when inserted from the “ideal” side ($\Delta_2 = 0$) from 60 kHz up to 2.1 MHz, Figure 5.

One can see that very small perturbations lead to uncertainty of extra length due to the errors of measurements. On

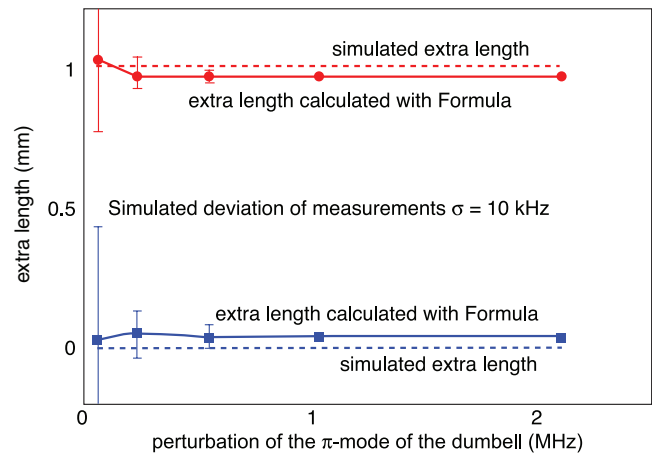


FIG. 5. Simulation of a dumbbell with extra lengths 0 and 1 mm.

the other hand, big perturbations give inaccurate values for the extra lengths calculated with formula (8).

We can treat the cup with the extra length $\Delta_1 = 1$ mm as an “Upper” cup or as a “Lower” cup. The choice of the upper or lower cup is conditional. R changes its sign when the dumbbell is turned over but also slightly changes its absolute value. The values of extra lengths calculated for these two possibilities are shown in Figure 6.

We will have practically the same graph if $\Delta_1 = 2$ mm, $\Delta_2 = 1$ (just values on the ordinate axis will increase by 1). So, Figure 6 shows that *the error is always smaller if the cup with bigger deviation of the π -mode is taken as the lower cup*, – accuracy in this case is about two times better.

If the cups have close dimensions, this difference between frequencies defined with swapped upper and lower cups becomes small (no difference if $R = 0$).

Why the old formula worked

For small values of R , the formulae (4) can be expanded, correct to first order, as

$$f_{\pi,U} = f_{\pi} \left[1 + \frac{f_{\pi}^2 - f_0^2}{f_{\pi}^2} \cdot \left(\frac{3R}{32} \right) \right], \quad (9)$$

$$f_{\pi,D} = f_{\pi} \left[1 - \frac{f_{\pi}^2 - f_0^2}{f_{\pi}^2} \cdot \left(\frac{5R}{32} \right) \right].$$

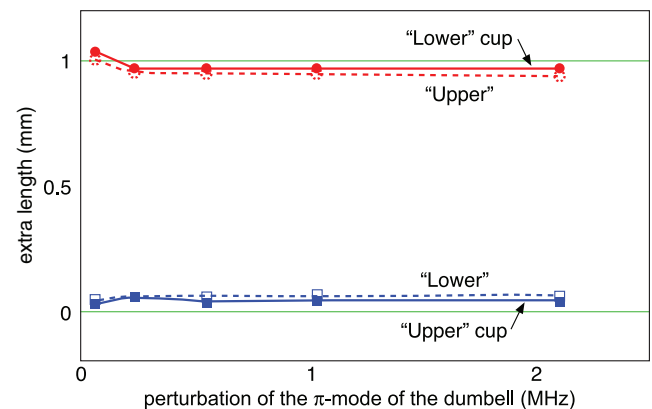


FIG. 6. Extra length calculated with Formula.

Analogously, the formulae (6) can be simplified as

$$\begin{aligned} f_{\pi,U}^* &= f_{\pi} \left[1 + \frac{f_{\pi}^2 - f_0^2}{f_{\pi}^2} \cdot \left(\frac{R}{8} \right) \right], \\ f_{\pi,D}^* &= f_{\pi} \left[1 - \frac{f_{\pi}^2 - f_0^2}{f_{\pi}^2} \cdot \left(\frac{R}{8} \right) \right]. \end{aligned} \quad (10)$$

If the dumbbell is measured twice (or even number of times) and Eq. (9) is used, the values in round brackets average, giving the same values as the formulae (10). Note, that R changes its sign when the dumbbell is turned upside down, as it is shown in Eq. (7). However, usage of the formulae (9) instead of (10) without such an averaging will give a $\pm 25\%$ error for the correction term standing after the unity.

This correction term can be neglected when both cups of the dumbbell have close frequencies ($f_{\pi,U} \approx f_{\pi,D} \approx f_{\pi}$) even if f_{π} differs from f_{target} and Δ_U and Δ_D are big, see Eq. (8). Again, in this case the old formulae will work.

However, when the frequency f_{π} of the dumbbell is close to the frequency f_{target} , for example when one cup is shorter and another one is longer than needed, usage of the old formulae will give up to 25% error.

A DUMBBELL MEASURING FIXTURE

To measure the resonant frequencies of a fabricated niobium dumbbell, a fixture with supporting hardware and software was constructed, Fig. 7. The system was inspired by the JLab system, with the most notable difference being the operating frequency (1300 MHz instead of 1500 MHz).³ The fixture was designed to accommodate completed end group measurements also. In the case of end groups, no perturbation was used since the cavity was comprised of a single half-cell. Two feedthroughs with antennas were placed in the upper and lower plates, and the RF measurement was done in transmission. For the end group, one antenna was replaced by a flexible conductor such that it was easily inserted into the cavity. In each case, the antenna length was trimmed such that the cavity was heavily undercoupled with a $Q_{ext} \approx 10^6$, giving $Q_l \approx Q_0$.

The measurement system consists of a HP85047A network analyzer (NA), a RF dumbbell fixture with copper contact fingers, and a Transducer Techniques load cell with analog readout. The NA and load cell were connected to a LABVIEW program which logs the frequency (f_0), quality factor (Q_0), and applied force. Q_0 and f_0 were determined by fitting the amplitude of S_{21} to the Lorentzian function while accounting for a constant direct transmission between antennas. LABVIEW was chosen to increase the measurement accuracy while simplifying the measurement and processing procedure.

The six measured frequencies comprised the 0 and π -mode, with and without perturbation in the upper and lower half-cells. These values were written to a file and then processed using MATLAB. The script calculates the individual π -mode frequencies according to the modified formulae (6). The program recognizes which half-cell has the biggest π -mode deviation and assigns this cup as “lower”, in spite of its physical location. The program also incorporates a correction for

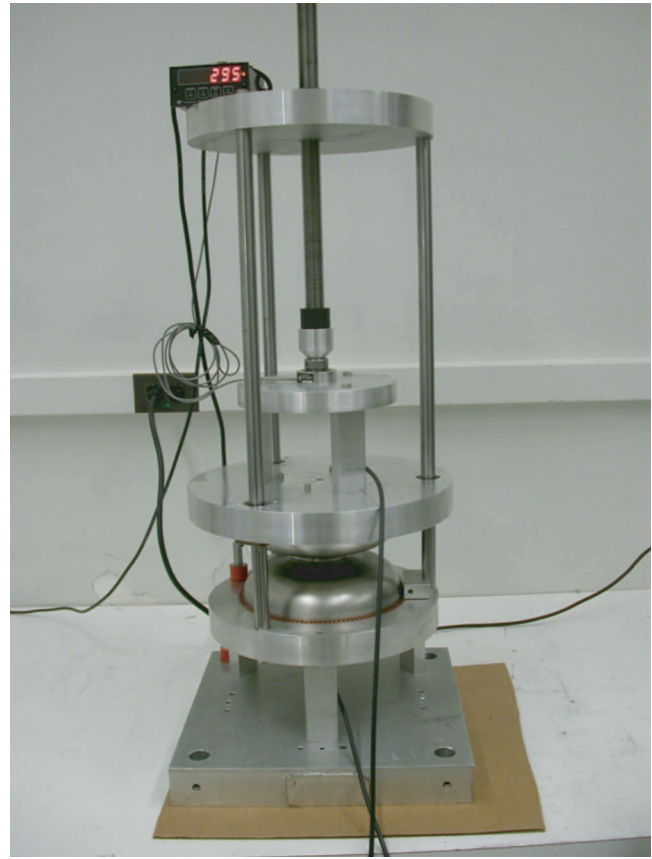


FIG. 7. Dumbbell measuring fixture.

ambient conditions: humidity, temperature, and atmospheric pressure as is described above.

The value of the frequency perturbation should be bigger than the error in measurement (10 kHz) but less than the difference between the 0 and π -mode frequencies (about 26 MHz). We have chosen our perturbation such that $\Delta f \approx 0.5$ MHz. The perturbing body is a cylinder 3.175 mm in diameter with a spherical top, and the total length of 6.5 mm. In order to guarantee reliability, the perturbation was fastened with a torque wrench to 10 inch · lb.

It should be noted here that there is a slight difference (0.15 mm) in the height of perturbation when it is inserted into the upper or lower disc. This difference causes a systematic error of 30 kHz. Besides, the upper disc has a sag about 0.025 mm, also causing an error, about 40 kHz. These errors add somewhat to the rms deviation but average out because the dumbbell is flipped during multiple measurements. Nevertheless, they should be eliminated for further measurements.

To obtain a reliable RF contact at the Nb/Cu joint, the fixture must compress the dumbbell between copper plates. The mechanical press comprised of linear bearings mounted on aluminum plates, sliding on case-hardened shafts. The press was manually driven by a 1-inch ACME screw. ANSYS simulations show that the force applied to the dumbbell should be kept below 350 lbs, in order to prevent inelastic deformation. Therefore, our operating pressure was 300 lbs. Elastic deformation will affect the resonant frequency of the cavity, but a linear extrapolation to zero pressure of the f_0 versus F curve

Date		2-Aug-11		<h1>CC37-CC38</h1>		
Measurement by:		PRC				
Temperature		21.9				
Ambient Pressure		735.8				
Humidity		60.0				
	Experiment1 :	Experiment2 :	Experiment3 :	Experiment4 :	mean	standard dev <kHz>
	cc37 on top	cc38 on top	cc37 on top	cc38 on top		
f_0	1270.410	1270.429	1270.396	1270.432	1270.417	17
f_0_p_cc37	1269.844	1269.831	1269.835	1269.833	1269.836	6
f_0_p_cc38	1269.824	1269.856	1269.811	1269.865	1269.839	26
f_pi	1296.323	1296.337	1296.306	1296.342	1296.327	16
f_pi_p_cc37	1295.823	1295.832	1295.815	1295.835	1295.826	9
f_pi_p_cc38	1295.824	1295.830	1295.811	1295.840	1295.826	12
f_pi_cc37	1296.432	1296.188	1296.414	1296.193	1296.307	134
f_pi_cc38	1296.213	1296.484	1296.198	1296.489	1296.346	163
Trim_cc37 <mil>	19.7	21.7	19.9	21.6	20.7	1.1
Trim_cc38 <mil>	21.5	19.3	21.6	19.3	20.4	1.3
mean load <lbs>	304.7	303.8	309.8	305.0	305.8	
mean Q	5555.0	5963.9	6015.9	5776.5	5827.8	
Notes:						
target frequency	1298.959					
trim parameter	128kHz					

FIG. 8. An example of the protocol of measurements.

found this deviation to be negligible compared to our machining tolerance. To overcome the dry-contact friction between components, a small mechanical vibrator was attached to the fixture. It was also helpful to gently rub the niobium dumbbell against the copper contact using a circular motion. To exclude the copper contamination of the niobium, a 30 min nitric acid etch of the equators was performed prior electron-beam welding. This removes copper without action on niobium.

These measures resulted in Q_0 's between 5000 and 7000. The theoretical value simulated in SLANS was about 7500 for both 0- and π -modes, given our geometry and material. We assumed that a Q_0 greater than 5000 indicates a reliable RF contact. Using the methods outlined above, we demonstrated repeatable frequency measurements with $\sigma = 10$ kHz, regardless of cavity orientation or re-insertion.

An example of the dumbbell measurement results is presented in Figure 8. Here, CC37 and CC38 are the names of cups the dumbbell is welded of. The value to be trimmed from each half-cell is shown in the last but one column: 20.7 and 20.4 mils (1 mil = 0.001 in. = 25.4 μ m).

CONCLUSION

A convenient method to transform cavity shape from the theoretical operating dimensions to the mechanical fabrication drawing dimensions is presented. This matrix method accounts for changes to the cells shapes due to cooling down to cryogenic temperature, mechanical tuning, and chemical etching. Frequency corrections due to atmospheric conditions are also analyzed.

Dumbbell cavities for the Cornell ERL multicell cavity were measured in a measuring fixture constructed to determine equator trimming lengths. Corrections were introduced into the formulae for calculation the individual half-cell frequencies. LABVIEW and MATLAB software was written for a semi-automatic measurements with a network analyzer, load

cell, and RF dumbbell fixture. Our system helped to control individual cell frequencies to within narrow limits: the first completed Cornell ERL 7-cell cavity has a field flatness of 88% immediately after fabrication and frequency deviation of 360 kHz that corresponds to an average deviation of less than 0.003 in. (75 μ m) per cell.¹⁷

ACKNOWLEDGMENTS

The authors are grateful to Professor G. Hoffstaetter for useful advices and support and to Professor M. Tigner who was the leading person in the first Cornell ERL multicell cavity production. The authors are also thankful to all the members of the team together with whom they were involved in this work.

¹G. Kreps, D. Proch, and J. Sekutowicz, in *Proceedings of the SRF'99*, Santa Fe, New Mexico, November 1999, p. 499.

²J. Iversen, Th. Buettner, A. Goessel, D. Klinke, G. Kreps, W.-D. Moeller, and C. Moeller, in *Proceedings of the SRF2009*, Berlin, Germany, September 2009, p. 786.

³F. Marhauser, *JLab SRF cavity fabrication errors, consequences and lessons learned*. (TJNAF, Newport News, VA, 2010), Paper No. JLab-TN-10-021.

⁴Actual operating temperature of the ERL cavity will be 1.8 K but this will change the contraction coefficient less than 1% that can be neglected. A bigger error would be due to the deviation of the room temperature at which the initial measurements are done but in any case it would be a correction of the second order.

⁵*Brookhaven National Laboratory Selected Cryogenic Data Notebook*, BNL, 10200-R, Vol. 1, IX-Q-1.

⁶Simulations with ANSYS for the ERL and LL cavities were done by Sam Posen.

⁷R. Geng, private communication (2012).

⁸J. Sears and J. Kaufman, private communication (2012).

⁹N. Valles and M. Liepe, in *Proceedings of the SRF2009*, Berlin, Germany, September 2009, p. 538.

¹⁰These measurements were done by Brendan Elmore.

¹¹S. Belomestnykh and V. Shemelin, *Nucl. Instrum. Methods Phys. Res. A* **595**, 293 (2008).

- ¹²D. G. Myakishev and V. P. Yakovlev, in *Proceedings of the PAC'95*, Dallas, Texas, USA, p. 2348.
- ¹³A. C. Strickland, RRB 1594, National Physical Laboratory, Dept. of Sci. and Ind. Research, 1942.
- ¹⁴*Reference Book on Electromagnetic Materials*, edited by K. A. Andrianov (GEI, Moscow – Leningrad, 1958), Vol. 1.
- ¹⁵S. An, Z. Liping, T. Yazhe, Y.-min Li, and Y.-S. Cho, *Rev. Sci. Instrum.* **79**, 104701 (2008).
- ¹⁶S. An, T. Yazhe, Z. Liping, Y.-min Li, G. Changyi and Y. S. Cho, in *Proceedings of the EPAC'08*, Genoa, Italy, July 2008, p. 823.
- ¹⁷Measurements of frequency and field flatness were done by Ben Bullock and Fumio Furuta.